

# Impact of initial mass functions on the dynamical channel of gravitational wave sources

Long Wang,<sup>1,2\*</sup> Michiko S. Fujii,<sup>1</sup> Ataru Tanikawa<sup>3</sup>

<sup>1</sup>*Department of Astronomy, School of Science, The University of Tokyo, 7-3-1 Hongo, Bunkyo-ku, Tokyo, 113-0033, Japan*

<sup>2</sup>*RIKEN Center for Computational Science, 7-1-26 Minatojima-minami-machi, Chuo-ku, Kobe, Hyogo 650-0047, Japan*

<sup>3</sup>*Department of Earth Science and Astronomy, The University of Tokyo, Japan*

Accepted –. Received –; in original form –

## ABSTRACT

Dynamically formed black hole (BH) binaries (BBHs) are important sources of gravitational waves (GWs). Globular clusters (GCs) are one of the major environments to produce such BBHs, but the total mass of the known GCs is small compared to that in the Galaxy, thus the fraction of BBHs formed in GCs is also small. However, this assumes that GCs contain a canonical initial mass function like that in the field stars. This might not be true because several studies suggest that extreme dense and metal-poor environment can result in top-heavy IMFs, where GCs may come from. Although GCs with top-heavy IMFs were easily disrupted or have become dark clusters, the contribution to the GW sources can be significant. Using a high-performance and accurate  $N$ -body code, PETAR, we investigate the effect of varying IMFs by carrying out four star-by-star simulations of dense GCs with the initial mass of  $5 \times 10^5 M_\odot$  and the half-mass radius of 2 pc. We find that the BBH merger rate does not monotonically correlate with the slope of IMFs. Due to a rapid expansion, top-heavy IMFs lead to less efficient formation of merging BBHs. The formation rate continuously decreases as the cluster expands due to the dynamical heating caused by BHs. However, in star clusters with a top-heavier IMF, the total number of BHs is larger, and therefore the final contribution to merging BBHs can still be more than clusters with the standard IMF, if the initial cluster mass and density is higher than the model we used.

**Key words:** methods: numerical – galaxies: star clusters: general – stars: black holes

## 1 INTRODUCTION

After LIGO/VIRGO detected gravitational wave (GW) events from mergers of stellar-mass black holes (BHs) and neutron stars (NSs) (Abbott et al. 2019, 2020), many studies have addressed on the origins of these events: isolated binaries through common envelope evolution (e.g. Giacobbo & Mapelli 2018; Belczynski, et al. 2020), through chemically homogeneous evolution (e.g. Marchant et al. 2016; Mandel & de Mink 2016) and stable mass transfer (e.g. Kinugawa et al. 2014; Tanikawa et al. 2020), hierarchical stellar systems (e.g. Antonini et al. 2014), open clusters (e.g. Ziosi et al. 2014; Kumamoto et al. 2019; Di Carlo et al. 2019; Banerjee 2020a), and galactic centers (e.g. O’Leary et al. 2009). Dense stellar systems like globular clusters (GCs) are considered as one of the major environment to form GW progenitors, binary black holes (BBHs), via few-body dynamical interactions (Portegies Zwart & McMillan 2000; Downing et al. 2010; Tanikawa 2013; Bae et al. 2014; Rodriguez et al. 2016a,b; Fujii et al. 2017; Askar et al. 2017; Park et al. 2017; Samsing et al. 2018; Hong et al. 2020). Although this dynamical channel can effi-

ciently produce GW events, the total contribution seems to be less than the events driven by the binary stellar evolution, because the total mass of GCs is a small fraction of the total galactic stellar mass. However, this assumes that the initial mass function (IMF) of the GCs is the same as that of the field stars, but it might not be the true because we do not have sufficient observational constraints on that yet.

Recently, several observational evidences indicate that extreme dense star forming region may have top-heavy IMFs, such as the Arches cluster in the Galactic center and 30 Doradus in the Large Magellanic Cloud, where the heavy-end of IMFs have exponent,  $\alpha \approx -1.7 \sim -1.9$ , (Lu et al. 2013; Schneider, et al. 2018; Hosek, et al. 2019). Therefore, it is natural to expect that the old and massive GCs in the Milky way may also contain top-heavy IMFs since its birth environment is very different from the present-day one. On the galactic scale, Zhang et al. (2018) found that for high-redshift ( $z \sim 2 - 3$ ) star-burst galaxies, a top-heavy (integrated) IMF is necessary to explain their star formation rate.

On the other hand, there is a puzzle related to the phenomenon of multiple stellar populations in GCs, called the “mass budget problem”. Observations show that several GCs have a more than half of enriched stellar populations (Milone

\* E-mail: long.wang@astron.s.u-tokyo.ac.jp

et al. 2017). The stellar evolution model to explain the formation of element-enriched stars, especially the AGB scenario, cannot produce sufficient materials to form such a large fraction of young populations (Bastian & Lardo 2018, and references there in). A top-heavy IMF is a natural solution for this (e.g. Wang et al. 2020).

With top-heavy IMFs, the strong wind mass loss from massive stars in the first 100 Myr significantly affects the density of the systems. Later on, the massive stars leave a large number of BHs in the star clusters, and they will also have a strong impact on the long-term evolution of the clusters. Indeed, it has been shown that GCs with top-heavy IMFs are much easier to expand and be disrupted (Chatterjee, Rodriguez, & Rasio 2017; Giersz, et al. 2019; Wang 2020; Weatherford et al. 2021).

Therefore, the dynamical evolution of GCs provides a strong constraint on the shape of IMFs. By using semi-analytic models, Marks et al. (2012) suggested that the shape of IMFs in GCs might depend on the metallicity and initial cloud density. Their model, however, ignored the dynamical impact of BHs, and thus they overestimated the slopes of IMFs for observed GCs. By comparing with scaled  $N$ -body models, Baumgardt & Sollima (2017) also argued that 35 observed dense GCs might not have top-heavy IMFs. However, GCs with top-heavy IMFs might have existed in the past but have already disappeared or have become dark clusters (Banerjee & Kroupa 2011). Thus, they cannot be directly observed today. Considering the large number of BHs existed there, the contribution of BBHs mergers might be significant.

Chatterjee, Rodriguez, & Rasio (2017), Giersz, et al. (2019) and Weatherford et al. (2021) have performed Monte-Carlo simulations of GCs to study the effect of top-heavy IMFs on the survival of GCs and the BBH mergers. However, Monte-Carlo method is not fully tested in the condition of top-heavy IMFs, where a large fraction of BHs exist. Rodriguez et al. (2016) compared the Monte-Carlo (the CMC code; e.g. Joshi, Rasio, & Portegies Zwart 2000) and the direct  $N$ -body methods (the NBODY6++GPU code; Wang et al. 2015) for million-body simulations of GCs. In this comparison, an abnormal oscillation of the core radius was found in the CMC simulation. Later, Rodriguez et al. (2018) showed that when BH number is large, the Joshi, Rasio, & Portegies Zwart (2000) code fails to produce the correct core evolution.

There are also studies using direct  $N$ -body methods, which must be more accurate than the Monte-Carlo simulations. Wang (2020) studied the effect of top-heavy IMFs on the survival of star clusters, but use a simplified two-component models without stellar evolution. Haghi et al. (2020) carried out a group of  $N$ -body models, but without a realistic number of stars like in the GCs. These models properly integrate individual stellar orbits and obtained correct dynamical evolution of GCs, but they cannot be used to study the BBH mergers. Therefore, it is necessary to carry out accurate star-by-star  $N$ -body simulations to study the GCs with top-heavy IMFs.

In this work, we carry out four models of GCs with the sufficient mass ( $5 \times 10^5 M_\odot$ ) and density (the half-mass radius is 2 pc). Different slopes of IMFs are used. In Section 2.1, we describe the  $N$ -body tool, PETAR, used in this study. The initial conditions of models are shown in Section 2.2. We describe the BBHs mergers and the dynamical evolution of the

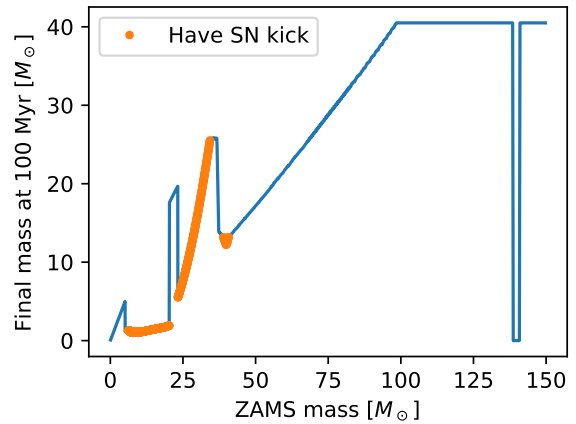


**Figure 1.** The initial-final mass relation of stars by applying the stellar evolution model from SSE. The yellow points indicate the remnants natal kick velocity of neutron stars and black holes after the supernova. Due to the fallback treatment, massive BHs have no kick velocity.

models in Section 3. Finally, we discuss our results and draw conclusions in Section 4 and 5.

## 2 METHODS

### 2.1 Petar

We use the PETAR code (Wang et al. 2020b) to provide the  $N$ -body models of GCs. This is a hybrid code that combines the particle-tree particle-particle (Oshino, Funato, & Makino 2011) and slowdown algorithm regularization (Wang, Nishida, & Makino 2020a) methods. Such combination reduces the computing cost compared to the direct  $N$ -body method while keep sufficient accuracy to deal with close encounters and few-body interactions. The code is based on the FDPS framework, which can achieve a high performance with the multi-process parallel computing (Iwasawa et al. 2016; Iwasawa, et al. 2020; Namekata et al. 2018).

The single and binary stellar evolution packages, SSE/BSE, are implemented in PETAR (Hurley, Pols, & Tout 2000; Hurley, Tout, & Pols 2002). We adopt the updated version of SSE/BSE from Banerjee et al. (2020b). The simulations use the semi-empirical stellar wind prescriptions from Belczynski et al. (2010), the “rapid” supernova model for the remnant formation and material fallback from Fryer et al. (2012) together with the pulsation pair-instability supernova (PPSN; Belczynski, et al. 2016). In Figure 1, we show the relation between zero-age main-sequence (ZAMS) masses and final masses of stars from 0.08 to  $150 M_\odot$  for  $Z = 0.001$ . With PPSN, massive stars which have the ZAMS mass above about  $100 M_\odot$  obtain the final mass of BHs fixed to  $40.5 M_\odot$ . This has a significant impact on the mass ratio distribution of BBHs, as shown in section 3. On the other hand, the fallback mechanism results in zero natal kick velocity for massive BHs with ZAMS mass of  $> 30 M_\odot$ . They can retain in the clusters after supernovae, while low mass BHs and most of neutron stars can gain high velocity kicks and immediately escape from the system.

**Table 1.** The name of  $N$ -body models with corresponding  $\alpha_3$  of IMFs and the number of stars ( $N$ )

Model	A1.5	A1.7	A2.0	A2.3
$\alpha_3$	-1.5	-1.7	-2.0	-2.3
$N$	182306	312605	581582	854625

## 2.2 Initial conditions

To specifically investigate how the shape of IMFs affect the formation and evolution of BBHs in GCs, we carry out four models by varying the  $\alpha_3$  in the Kroupa (2001) IMF with a multi-component power-law shape:

$$\begin{aligned} \xi(m) &\propto m^{\alpha_i} \\ \alpha_1 &= -1.3, \quad 0.08 \leq m/M_\odot < 0.50 \\ \alpha_2 &= -2.3, \quad 0.50 \leq m/M_\odot < 1.00 \\ \alpha_3, & \quad 1.00 \leq m/M_\odot < 150.0. \end{aligned} \quad (1)$$

The value of  $\alpha_3$  and corresponding model names are listed in Table 1. A2.3 has the canonical value of  $\alpha_3$  while all the others correspond to different degrees of top-heavy IMFs. The maximum value of  $\alpha_3$  is chosen to be 1.5. We use the full mass range of IMF, where the minimum and the maximum masses of stars are 0.08 and 150  $M_\odot$ , respectively. For the metallicity, which determines the stellar evolution (mass loss) of stars, we adopt a typical value for GCs,  $Z = 0.001$ .

For all models, we adopt Plummer profile to set up the positions and velocities of individual stars. We fix the initial total mass to be  $5 \times 10^5 M_\odot$  and the initial half-mass radius,  $r_{h,0}$ , to be 2 pc. Thus, our models have a mass and density as high as those typical for observed GCs. In fact, the density of our model is higher than that of the previous largest DRAGON GC model (Wang et al. 2015). Thus, our simulations are still time-consuming even using the PETAR.

As a start, we assume no primordial binaries in these models. This simplifies the discussion since we can purely focus on the dynamical formation of BBHs. On the other hand, it is easier to perform the models. We do not apply the galactic potential either, but we remove unbounded stars when they reach more than 200 pc far from the cluster centre.

## 3 RESULTS

We do not intend to create realistic GC models with primordial binaries and galactic tidal field, but focus on the theoretical studies of the BBHs in GCs. Thus, we only evolve our models up to 3 Gyr instead of Hubble time, using the available computing resource. However, this already covers about 10 initial half-mass relaxation time of the systems, thus it is sufficient for analysis.

### 3.1 BBH mergers

In our simulations, we do not model BBH mergers via the effect of general relativity. We instead detect all BBHs that are potential GW mergers in the post-process using the snapshots of the simulations. We apply the following two steps to obtain the BBH mergers.

**Table 2.** The number of BBH merger candidates ( $N_{\text{cand}}$ ), mergers inside GCs ( $N_{\text{in}}$ ) and escaped mergers ( $N_{\text{out}}$ ) up to the 3 Gyr evolution of GCs.

Model	A1.5	A1.7	A2.0	A2.3
$N_{\text{cand}}$	20	10	30	43
$N_{\text{in}}$	0	1	3	3
$N_{\text{out}}$	3	3	3	4

Firstly, we estimate merger timescale for each binary based on the formula provided by Peters (1964):

$$\begin{aligned} t_{\text{gw}} &= \frac{12}{19} \frac{c_0^4}{\beta} \int_0^{e_0} \frac{e^{29/19} [1 + (121/304)e^2]^{1181/2299}}{(1 - e^2)^{3/2}} de \\ c_0 &= \frac{a_0(1 - e_0^2)[1 + (121/304)e_0^2]^{870/2299}}{e_0^{12/19}} \\ \beta &= \frac{64}{5} \frac{G^3 m_1 m_2 (m_1 + m_2)}{c^5}. \end{aligned} \quad (2)$$

By calculating  $t_{\text{gw}}$  of BBHs in the snapshots with the time interval of 0.25–1 Myr, we select the merger candidates which have the actual (delayed) merging time  $t_{\text{merge}} \equiv t_{\text{gw}} + t < 12\text{Gyr}$ , where  $t$  is the physical time of the cluster when  $t_{\text{gw}}$  is calculated.

However, these candidates may not actually merge because BBHs with high eccentricities can be perturbed by their surrounding stars, if they are still in the cluster. The orbits of BBHs can also dramatically change after a strong few-body interaction. If the eccentricity decreases,  $t_{\text{gw}}$  can significantly increase. Thus, in the second step, we look the evolution of each candidate and check whether they escape from the system or merge before their  $t_{\text{gw}}$  increase.

The numbers of candidates and confirmed mergers for each model are shown in Table 2. We can notice that the number of candidates does not monotonically depends on the  $\alpha_3$  of IMFs. More top-heavy the IMF is, less  $N_{\text{cand}}$  tend to be, except for that of the A1.5 model (the most top-heavy one). The A1.5 model has more  $N_{\text{cand}}$  than that of the A1.7. We will explain the reason in Section 3.2.

Figure 2 shows the evolution of semi-major axis ( $a$ ) of all BBHs detected in the snapshots of our simulations. The candidates, inner and escaped BBH mergers are shown together. In this figure, we can identify two types of BBHs, the soft and hard ones separated by  $a \approx 10^3$  AU. Due to the Heggie-Hills law (Heggie 1975; Hills 1975), soft binaries are easily disrupted by close encounters, but hard binaries become tighter. This is seen in the Figure 2. Soft BBHs randomly appear and vanish, while hard binaries continuously evolve harder following a clear trace of decreasing  $a$ . Typically, only one or two hard BBHs appear at one time because binary-binary encounters tend to break softer binaries. Once their  $a$  becomes small enough, a strong encounter can eject them out of the GCs, and they disappear in the Figure. Then new hard BBHs form and repeat the same process.

From the A2.3 model, we can identify a clear trend that BBHs with large masses prefer to form first. Once they escape, BBHs with lower masses form and escape one by one. This feature results in a clear difference in the mass ratio distribution of BBH components depending on IMFs, as shown in Figure 3. As more top-heavy IMFs have larger fractions of stars with the ZAMS masses above  $100M_\odot$ , more equal-mass

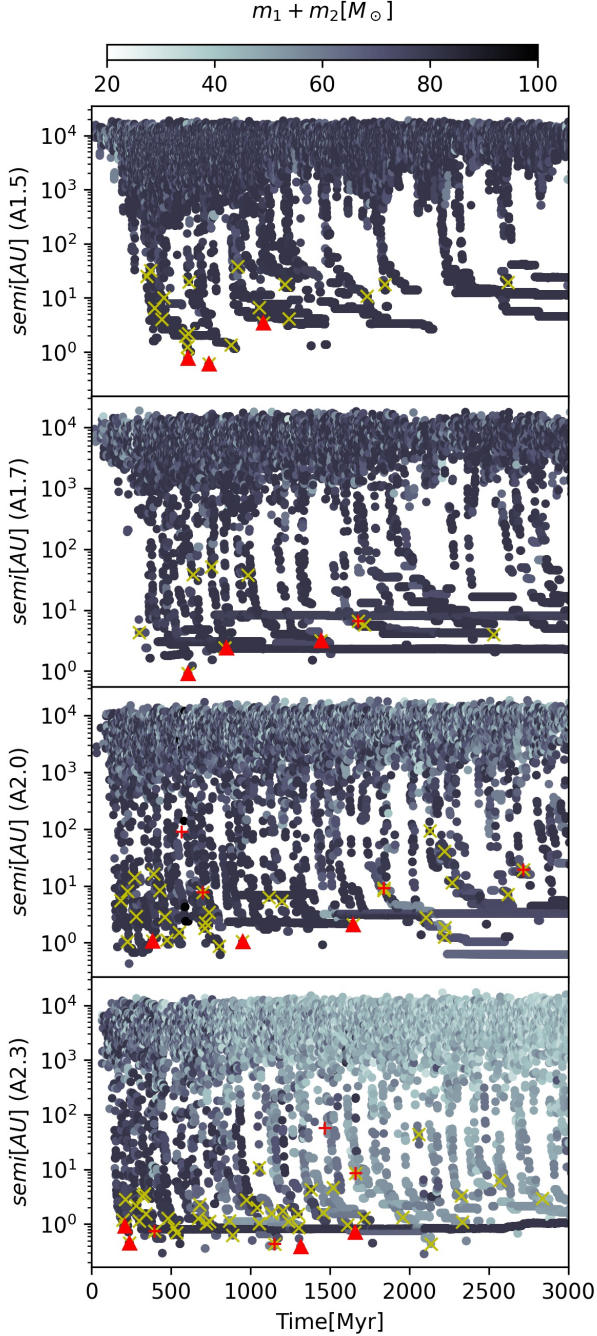


**Figure 2.** The evolution of semi-major axes of all BBHs in the four models. The gray scale indicates the total masses of BBHs. The yellow “x” represents the merger candidates. The red triangles and red crosses represents escaped mergers and mergers inside GCs.

BHs of  $40.5M_{\odot}$  form as a result of the PPSN. These most massive BHs form binaries first. Thus the BBH mergers in top-heavy IMFs tend to have  $q$  closer to unity.

Another major feature shown in Figure 2 is the increase of minimum semi-major axis (maximum binding energy), especially in the A1.5 model. As a result, it becomes more difficult to form tight BBHs in the later evolution of GCs. This is reflected on the  $N_{\text{cand}}$  as a function of time. Most of the candidates form in the first 1000 Myr in the A1.5 model, and

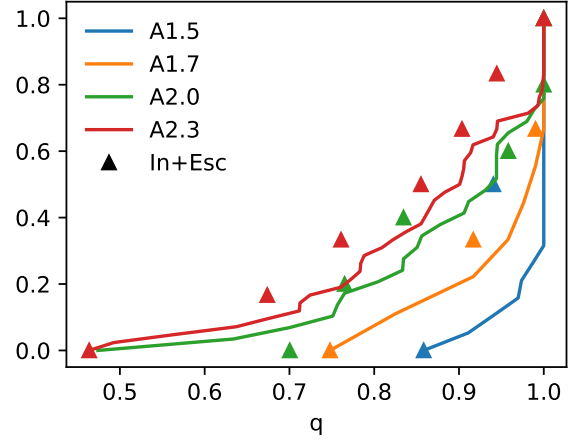


**Figure 3.** The cumulative distribution of mass ratio  $q$  of two components in BBH candidates (lines) and confirmed (triangles) mergers.

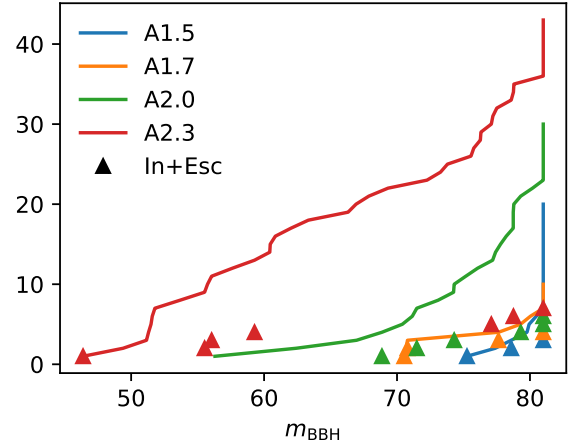


**Figure 4.** The cumulative distribution of the masses of BBHs candidates (solid curves) and confirmed ones (triangles)

the formation rate significantly decreases after 2000 Myr. In Section 3.3, we explain why the minimum semi-major axis increases by analyzing the escape velocities of GCs.

In Figure 4, we show the cumulative distribution of the masses of BBH merger candidates and confirmed ones. There are only a few confirmed mergers with  $m_{\text{BBH}} < 60M_{\odot}$  in the A2.3 model. In A1.5 models, on the other hand, most of mergers have  $m_{\text{BBH}} = 81M_{\odot}$  with the mass of each component being  $m_{\text{BBH}} = 40.5M_{\odot}$  due to the PPSN. Thus, clusters with a more top-heavy the IMF form more massive mergers.

In Figure 5, we show the cumulative distribution of  $t_{\text{gw}}$  and  $t_{\text{merge}}$  for BBH merger candidates and confirmed ones for all models. While mergers inside GCs have a short merger time ( $t_{\text{gw}} < 1$  Myr and  $t_{\text{merge}} < 3$  Gyr), most escaped mergers have a relatively long merger time ( $t_{\text{gw}} > 1$  Gyr and  $t_{\text{merge}} = 1 - 10$  Gyr). Therefore, the escaped mergers from all models with different IMFs can be detected today.



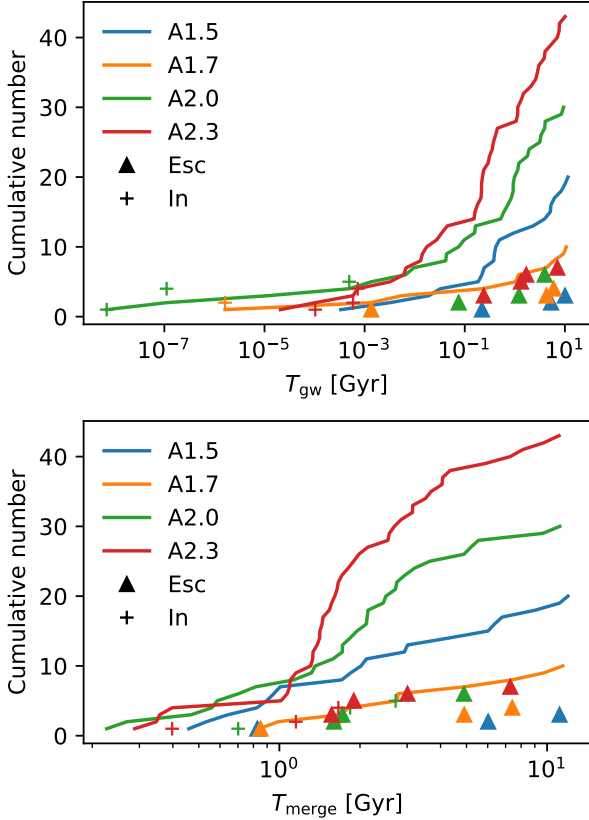


**Figure 5.** The cumulative number of BBH merger candidates (solid curves), mergers inside GCs (crosses) and escaped mergers (triangles) vs.  $t_{\text{gw}}$  (upper panel) and  $t_{\text{merge}}$  (lower panel).

### 3.2 Effect of stellar evolution on dynamics

The stellar evolution, especially wind mass loss of massive stars in the first 100 Myr, has a significant impact on the later-on and long-term evolution of GCs. Especially, the mass loss with a top-heavy IMF is more intense due to the larger fraction of massive stars. This significantly affects the central density of GCs. As shown in Figure 6, the core radii ( $R_c$ ) in the first 100 Myr become larger with more top-heavy IMFs. Once most massive stars become compact remnants, such the strong wind mass loss stops. Then,  $R_c$  starts to shrink and finally core collapse happens. Figure 6 shows that the A1.5 model contracts the deepest during the core collapse, probably due to the larger masses of the BHs, and the longer distance of sinking. This causes the densest core between 350 – 450 Myr compared to those of the other models. Such high density might be the reason why the A1.5 model has a more number of BBH merger candidates compared to that of the A1.7 model. Figure 2 shows that many of BBH merger candidates appear around 400 Myr in the A1.5 model. This is consistent with the feature of core collapse.

### 3.3 Expansion due to BH heating

Due to the larger masses of BHs compared to those of stars, BHs have a strong impact on the long-term evolution of star cluster (Breen & Heggie 2013). In star clusters including BHs, massive BHs sink into the cluster center due to the dynamical

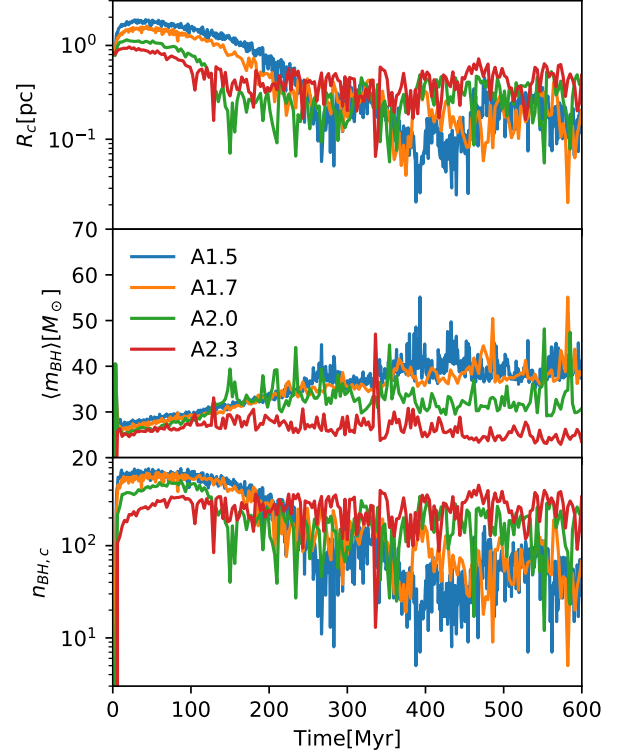


**Figure 6.** The evolution of core radii ( $R_c$ ); averaged masses ( $\langle m_{\text{BH},c} \rangle$ ) and numbers of BHs ( $N_{\text{BH},c}$ ) inside  $R_c$ . BBHs are counted as single objects.

cal friction (mass segregation) and form a dense subsystem. After that, the core collapse of the BH subsystem happens and drive the formation of BBHs, which heats the systems via few-body interactions. As a result of the energy-balanced evolution, the halo composed of light stars expands. When more BHs exist, the expansion is faster (see also in Giersz, et al. 2019; Wang 2020). This can be identified in Figure 7, in which the evolution of the half-mass radii of non-BH objects ( $R_{\text{h,noBH}}$ ) and BHs ( $R_{\text{h,BH}}$ ) are compared for all models.

In the first 300 Myr,  $R_{\text{h,BH}}$  decreases due to the mass segregation, and later it increases due to the BH heating. On the other hand,  $R_{\text{h,noBH}}$  always increases. The stronger stellar mass loss in more top-heavy models result in larger  $R_{\text{h,BH}}$  and  $R_{\text{h,noBH}}$  in a short time ( $< 100$  Myr). This is similar to the evolution of the core radii shown in Figure 6. As a result of stronger BH heating during the long-term evolution after 300 Myr,  $R_{\text{h,BH}}$  and  $R_{\text{h,noBH}}$  increase faster in the more top-heavy models.

According to Heggie-Hill law, the boundary semi-major axis between soft and hard BBHs depend on the masses of BHs and local velocity dispersion:

$$a_{\text{s/h}} = \frac{Gm_1m_2}{\langle m \rangle \sigma^2} \quad (3)$$

We check the density ( $\rho_{\text{BH}}$ ) of and 3D velocity dispersion ( $\sigma_{\text{BH}}$ ) of the BHs within 10% Lagrangian radii of all BHs and  $R_c$  of the BH subsystem. The results are shown in Figure 8. We find that  $\rho_{\text{BH}}$  inside  $R_{\text{lagr,BH},10\%}$  varies, as the slope of the IMF changes, i.e., models with more top-heavy IMFs have lower central densities. This is consistent with the behaviour

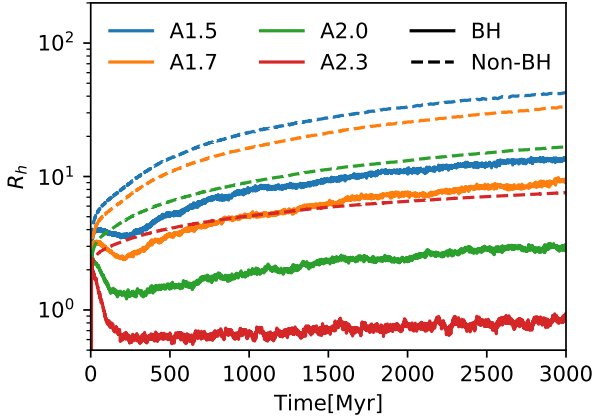


**Figure 7.** The evolution of half-mass radii of non-BH objects ( $R_{h,\text{noBH}}$ ; dashed curves) and BHs ( $R_{h,\text{BH}}$ ; solid curves).

of  $R_{h,\text{BH}}$  (see Figure 6). In contrast,  $\rho_{\text{BH}}$  inside  $R_c$  are very similar among all models, different from the behaviour on a larger distance scale.

We can divide the models into two groups, A1.5/A1.7 and A2.0/A2.3, based on the values of  $\sigma_{\text{BH}}$  within  $R_{\text{lagr,BH},10\%}$  or  $R_c$ . There is a gap of  $\sim 2$  pc/Myr in  $\sigma_{\text{BH}}$  between the two groups. Models with more top-heavy IMFs have smaller  $\sigma_{\text{BH}}$ , thus their  $a_{s/h}$  are larger due to Equation 3. This is consistent with the hard-soft boundaries shown in Figure 2.

As clusters expand,  $\sigma_{\text{BH}}$  continues decreasing for all models, and  $a_{s/h}$  increases. This is identified in the A1.5 and A1.7 models in Figure 2. In the A2.0 and A2.3 models, on the other hand, we can clearly see that the masses of BBHs decrease with time. This balances the effect of decreasing  $\sigma_{\text{BH}}$ , and thus the change of  $a_{s/h}$  is not obvious for these two models.

The key quantity that controls the minimum semi-major axis of binaries is the central escape velocity of star clusters. As the semi-major axis of a hard binary shrinks, the binary can gain larger kinetic energy (larger kick to the center-of-mass velocity) after a strong encounter. This process finally causes the ejection of the binary from the center of the cluster after a strong encounter. If the ejection velocity is below the escape velocity, the dynamical friction bring it back to the center. The binary can continue to encounter with others and become harder, until the next strong encounter ejects it again. Therefore, the escape velocity of star clusters limits the minimum semi-major axis of hard binaries that can be reached by few-body encounters.

Based on the mechanism described above, we can estimate GW merger timescale ( $t_{\text{gw}}$ ) of an ejected BBH, which should be an indicator for  $t_{\text{gw}}$  of BBHs in a star cluster. According to Equation 2 (Peters 1964),  $t_{\text{gw}} \propto a_{\text{esc}}^4/m_1^3$ , where  $a_{\text{esc}}$  is the semi-major axis of an ejected BBH, and we assume  $m_2 = m_1$  for the BBH. Since an ejected BBH has an internal velocity of  $\sim v_{\text{esc}}$ ,  $a_{\text{esc}} = Gm_1/(2v_{\text{esc}}^2)$ , and  $t_{\text{gw}} \propto m_1/v_{\text{esc}}^8$ . Eventually, an ejected BBH has larger  $t_{\text{gw}}$  when it contains heavier BHs, and when it is ejected from a star cluster with a smaller escape velocity.

In Figure 9, we estimate the central escape velocity of the Plummer model,

$$v_{\text{esc}} = \sqrt{2 \times 1.305 G \frac{M}{R_h}}, \quad (4)$$

where  $M$  is the total mass of the system. Due to the larger  $R_h$  in models with top-heavy IMFs, their  $v_{\text{esc}}$  is smaller. Moreover, their BHs are heavier in models with more top-heavy IMFs. Therefore, it is more difficult to form BBH mergers there, although the number of BHs is much larger. On the other hand,  $v_{\text{esc}}$  decreases, as the cluster expand. This explains why the minimum semi-major axis increases as shown in Figure 2 especially for the A1.5 model, because the masses of BBHs keeps a similar value up to 3 Gyr. In the case of the A2.3 model, masses of BBHs decrease, while the minimum semi-major axis does not show a strong increasing trend.

Since models with top-heavy IMFs have a stronger expansion and keep heavier BHs inside the clusters, the efficiency of forming BBH mergers decrease faster. Therefore, with the same initial total mass and size, the BBH merger rate is actually lower in the GCs with top-heavy IMFs. If the cluster with a top-heavy IMF was under a strong tidal field, the decrease of  $v_{\text{esc}}$  would be faster, thus it would be more difficult for the cluster to generate merging BBHs. However, if the cluster was initially denser and more massive, it could survive up to Hubble time and continue to generate merging BBHs all the time. In such a case, the cluster with a top-heavy IMF contains a large number of BHs, and therefore the total contribution of BBH mergers can be significantly larger than that in a GC with the same mass and size but a top-light IMF. Such ‘dark clusters’ has been studied in the Monte-Carlo simulations (Weatherford et al. 2021).

### 3.4 Mass loss

The stellar wind and BH heating drive the mass loss of star clusters in the early and later phase, respectively. Figure 10 (upper panel) shows the time evolution of the total masses of BH and non-BH components in the four models. After 100 Myr, the A1.5 model loses about 60% of the initial mass due to stellar-wind mass loss, while the A2.3 model loses only 30%. Therefore, the impact of the stellar evolution is more significant in star clusters with more top-heavy IMFs. Such strong mass loss later drives the fast expansion of the system as shown in Figure 6 and 7. Since our models do not have tidal field but simply remove unbound stars above 200 pc, the A1.5 model still survives and keeps about 34% initial mass at 3 Gyr. In the realistic condition, where the galactic tidal field play a role, the clusters with top-heavy IMFs tend to dissolve much faster than our current models (Wang 2020).

Breen & Heggge (2013) and Wang (2020) have found that the mass fraction of BHs in the system ( $M_{\text{BH}}/M$ ) evolve depending on the initial ratio and the tidal field in the following mechanism. Since BHs are centrally concentrated, they are not directly affected by the tidal field. Thus the tidal evaporation of BHs can be neglected. As mentioned in Section 3.3, strong close encounters between hard BBHs and intruders can eject BHs from the cluster. This is the major scenario that causes the mass loss of BHs.

On the other hand, light stars in the halo are truncated by the tidal field. When BH heating exists, this process is accelerated (Breen & Heggge 2013; Giersz, et al. 2019; Wang 2020). In the lower panel of Figure 10, we can identify the two different evolution trend of  $M_{\text{BH}}/M$ . In the A2.3 model,  $M_{\text{BH}}/M$  decreases with time, and finally most of BHs will be ejected out from the clusters. The core collapse of light stars will happen, and a GC with a dense core will appear.

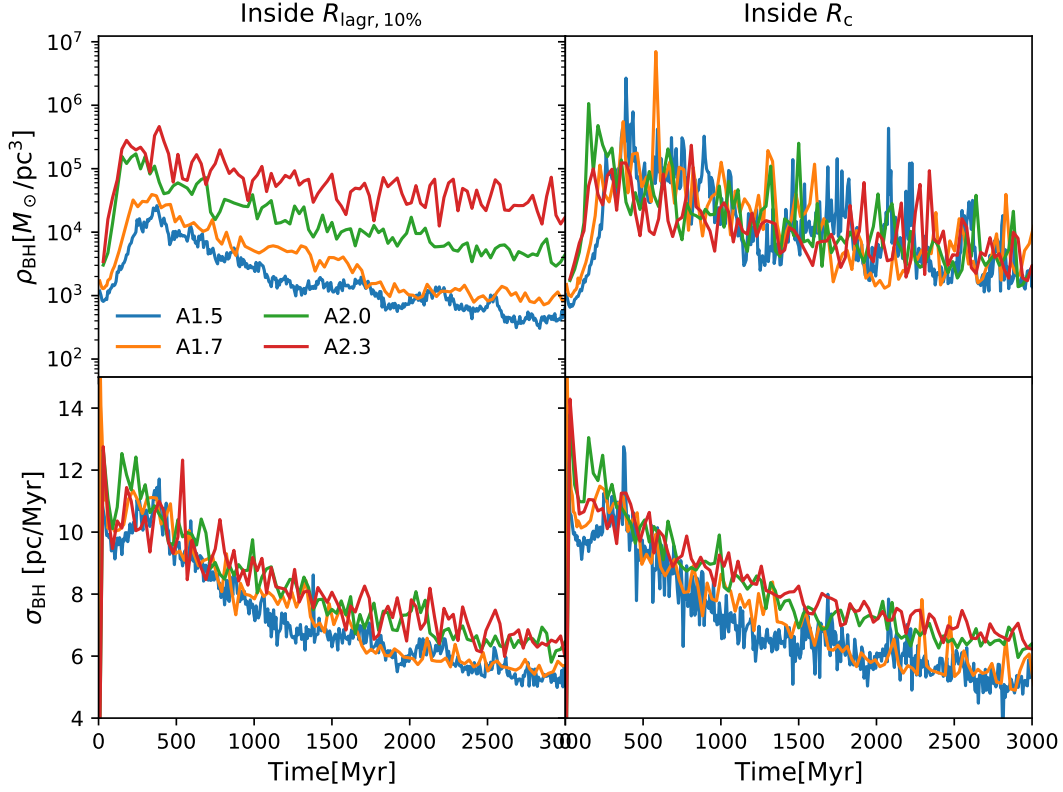


**Figure 8.** The evolution of density of BHs ( $\rho_{\text{BH}}$ ) and 3D velocity dispersion of BHs ( $\sigma_{\text{BH}}$ ) within 10% Lagrangian radii ( $R_{\text{lagr}, \text{BH}, 10\%}$ ) and  $R_c$

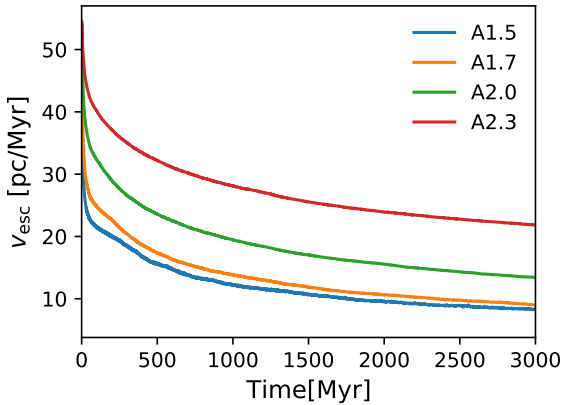


**Figure 9.** The evolution of the central escape velocity of the models

In contrast,  $M_{\text{BH}}/M$  in the A1.5 and A1.7 models increases with time. This means that light stars will finally evaporate from such clusters and that dark clusters form. In a strong tidal field, the mass loss of light stars is faster and such process can be accelerated. The A2.0 model is in the transition region.

With a two-component simplified model, Wang (2020) found that the mass loss rate of BHs,  $M_{\text{BH}}(t)/M_{\text{BH}}(0)$ , simply depends on the mass segregation time of heavy components ( $t_{\text{ms}}$ ) in isolated clusters, but the dependence becomes complex if a tidal field exists. In our models with stellar evo-

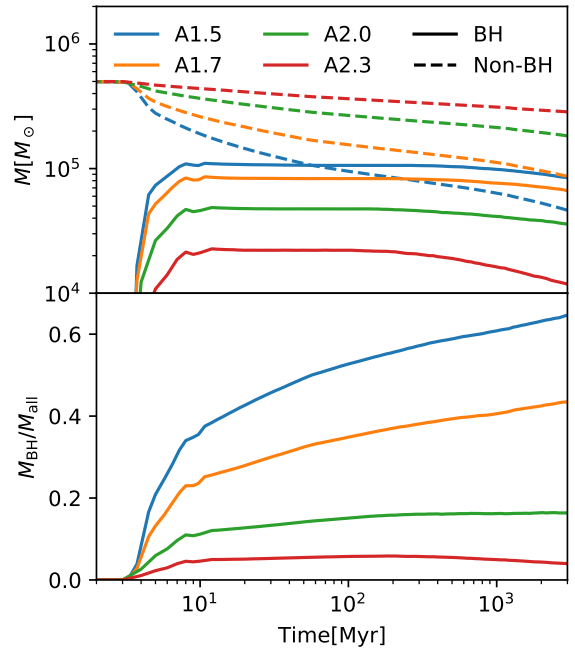


**Figure 10.** The evolution of total masses of BH and non-BH components (upper panel) and mass ratio between these two (lower panel).

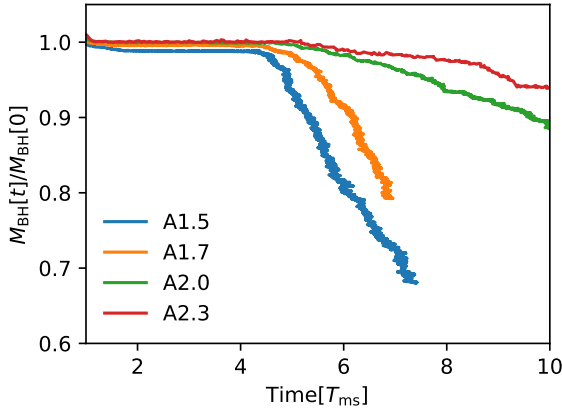


**Figure 11.** The evolution of total mass of BHs,  $M_{\text{BH}}(t)$ . The mass is normalized by using the value at 100 Myr. Time is in the unit of  $t_{\text{ms}}$  (eq. 5).

lution and IMFs, even without tidal field,  $M_{\text{BH}}(t)/M_{\text{BH}}(0)$  does not simply depend on  $t_{\text{ms}}$  as shown in Figure 11. In two-component models, the definition of  $t_{\text{ms}}$  is simple:

$$t_{\text{ms}} = \frac{m_1}{m_2} t_{\text{rh},1}, \quad (5)$$

where the relaxation time of light component has the form

$$t_{\text{rh},1} = 0.138 \frac{N^{1/2} R_{\text{h}}^{3/2}}{m_1^{1/2} G^{1/2} \ln \Lambda}. \quad (6)$$

However, with a mass function, the precise definition of  $t_{\text{ms}}$  is difficult to determine. Here we use the averaged mass of non-BH and BH components as a replacement of  $m_1$  and  $m_2$  in Equation 5 and 6. Theoretical studies have shown that when multi components exist, the diffusion coefficients need to be properly averaged to obtain the correct relaxation time (Spitzer & Hart 1971; Antonini & Gieles 2019; Wang 2020). Thus, using averaged mass is not accurate to calculate  $t_{\text{rh},1}$ . Especially, since the mass functions are different among the four models, there probably need to introduce a correction factor  $\psi$  to  $t_{\text{rh},1}$ , similar to the case in the two-component models done in Wang (2020). Moreover, the stellar evolution introduces another complexity. Thus, it is reasonable to see that  $M_{\text{BH}}(t)/M_{\text{BH}}(0)$  does not simply depends on  $t_{\text{ms}}$ . Instead, Figure 11 shows that the mass loss rate of BHs is faster when IMF is more top-heavy. This again indicates that star clusters with top-heavy IMFs evolve faster.

### 3.5 Energy-balanced evolution

Breen & Heggie (2013) established a theory to describe the long-term evolution of star clusters with BH subsystems. The key idea is based on the energy-balanced evolution of star clusters (Hénon 1961, 1975). After the BH subsystem form in the center of star clusters due to the mass segregation, BHs drive the binary heating process and provide the energy to support the whole system. The Hénon’s principle suggests that the energy flux from the center (BH subsystem) should balance the one required by the global system. This can be described by (Eq. 1 in Breen & Heggie 2013)

$$\frac{E}{t_{\text{rh}}} \approx k \frac{E_{\text{BH}}}{t_{\text{rh},\text{BH}}}, \quad (7)$$

where  $E_{\text{BH}}$  and  $E$  are the total energy of the BH subsystem and the global system respectively;  $t_{\text{rh}}$  and  $t_{\text{rh},\text{BH}}$  are the two-body relaxation times measured at  $R_{\text{h}}$  and  $R_{\text{h},\text{BH}}$ , respectively.

This relation constrains the behaviour of BHs, i.e., the density of the BH subsystem, the formation rate of BBHs and the escape rate of BHs are controlled by the global system (light stars), not the BH subsystem itself. By extending the Breen & Heggie (2013) theory to top-heavy IMFs, Wang (2020) found that when a large fraction of BHs exist, the energy balance is different from the description of Equation 7. To properly measure the energy balance between the central BH subsystem and the global system, the correction factor  $\psi$  is required to define the relaxation time more appropriately (as discussed in Section 3.4). In Wang (2020),  $\psi$  is defined as

$$\psi = \frac{\sum_k n_k m_k^2 / v_k}{\langle n \rangle \langle m \rangle^2 / \langle v \rangle}, \quad (8)$$

where  $n_k$ ,  $m_k$  and  $v_k$  are the number density, the mass of one object and the mean square velocity of the component  $k$ ,  $\langle n \rangle$ ,  $\langle m \rangle$  and  $\langle v \rangle$  represent the average values of all components, respectively.

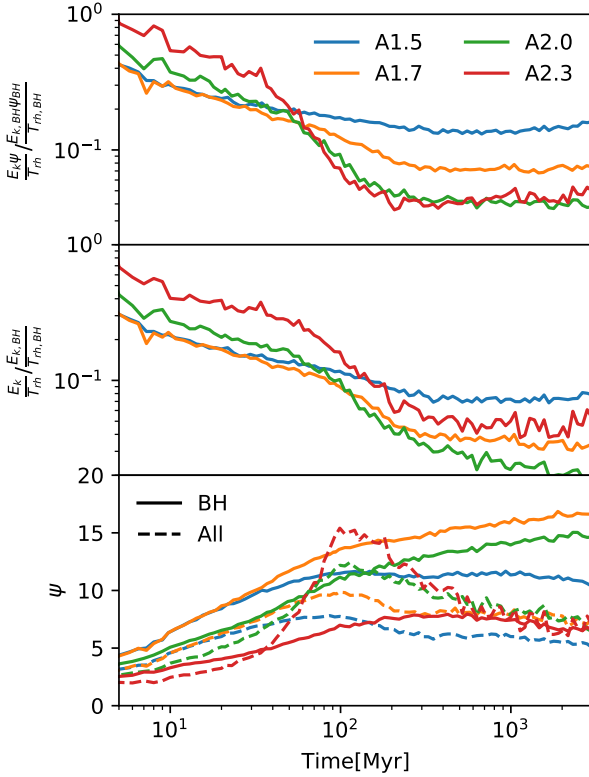
Figure 1 in Wang (2020) shows that if  $\psi$  is not included,  $k$  in Equation 7 is not a constant, but depending on the individual and total masses of BHs. With the correction factor  $\psi$ , the value of  $k$  becomes constant for most models with  $M_{\text{BH}}/M < 0.4$ . The  $N$ -body models in Wang (2020) are low-mass clusters with only two mass components and no stellar evolution. With more realistic models, we provide a similar analysis by treating BHs and non-BHs as two components.

Figure 12 shows the evolution of energy flux rate (measured at  $R_{\text{h}}$  and  $R_{\text{h},\text{BH}}$ ) with and without  $\psi$  factor, and the evolution of  $\psi$  of all objects and BHs, respectively. With the correction of  $\psi$  to  $t_{\text{rh}}$  (the upper panel), the A2.0 and A2.3 models show the same ratio of energy flux, while the A1.5 and A1.7 models have higher ratios. Without correction (the middle panel), on the other hand, there is no common ratio among all four models. The lower panel shows the evolution of  $\psi$  measured at  $R_{\text{h}}$  and  $R_{\text{h},\text{BH}}$ . The value of  $\psi[R_{\text{h},\text{BH}}]$  initially increases for all models but more rapidly for the top-heavy models (the A1.5 and A1.7 models). Then it slightly decreases after 1 Gyr for the A2.0 and A2.3 models. The value of  $\psi[R_{\text{h}}]$  also increases in the beginning. For the A2.3 model, it significantly at around 100 Myr and then decreases to a similar value to  $\psi[R_{\text{h}}]$ . For the other models, it also peaks at around 100 Myr but has a lower value compared to  $\psi[R_{\text{h},\text{BH}}]$  later on. The analysis here ignores the issue of the internal  $\psi$  factors for the BH and non-BH components discussed in Section 3.4. But the result is consistent with what is found in Wang (2020).

## 4 DISCUSSION

In this work, we did not include the general relativity effect on BH orbits during the simulation, but considered it in the post-process analysis to detect the BBH mergers. We therefore cannot detect hierarchical mergers, which can be the sources for massive BHs detected by LIGO/VIRGO (Abbott et al. 2019, 2020). With the same reason, in our simulations, we also did not find intermediate-mass black holes (IMBHs), which





**Figure 12.** The evolution of energy flux rate (measured at  $R_h$  and  $R_{h,BH}$ ) with (the upper panel) and without (the middle panel) the correction factor,  $\psi$ , respectively.  $\psi$  measured at  $R_h$  and  $R_{h,BH}$  are shown in the bottom panel.

are discussed in (Portegies Zwart et al. 2004; Giersz, et al. 2015; Rizzuto et al. 2020).

Without primordial binaries, these models probably underestimate the BBH merger rates, since primordial binaries can lead to stellar-evolution-driven formation of BBHs. The exchange of components via dynamical encounters between primordial binaries and BHs can also generate BBHs. This channel is also missed in our current simulations.

By including the tidal field, the survival timescale of A1.5 and A1.7 can be much shorter. This can also affect the BBH merger rates. In the future work, we will carry out new models by improving all these aspects.

Since we include PPSN in our simulations, the models with top-heavy IMFs have a large fraction of equal-mass BBHs ( $40.5M_\odot$ ). This can be changed by adopting the metallicity different from  $Z = 0.001$  or different stellar-evolution models for massive stars. Thus, our finding of the mass ratio distribution of BBHs cannot represent all kinds of conditions. But the trend, i.e., top-heavy IMFs tend to lead to a higher mass ratio of BBHs, would be general even if the stellar evolution models was changed.

## 5 CONCLUSIONS

In this work, we carry out four star-by-star  $N$ -body simulations of GCs with different IMFs, and initially  $M = 5 \times 10^5 M_\odot$  and  $R_h = 2$  pc. We find that the formation rate of BBH mergers depends on the stellar evolution and dynamical

process (core collapse and BH heating) in a complicated way. There is no monotonical correlation between the slope of IMF ( $\alpha_3$ ) and the number of (potential) BBH mergers (Figure 2, Table 2). The stronger stellar-wind mass loss in the first 100 Myr leads to a faster expansion of GCs with more top-heavy IMFs. As the escape velocity is lower in more top-heavy models, merging BBHs less efficiently form in these clusters, although the number of BHs is much higher. However, the A1.5 model, which shows a deeper core collapse after expansion, can produce a burst of BBH merger candidates at the momentum of the core collapse (Figure 2,6).

During the long-term evolution, it is more difficult to form BBH mergers in GCs with more top-heavy IMFs because they expand faster. This trend can be identified from the evolution of the minimum semi-major axis of hard BBHs shown in Figure 2. Therefore, with the same initial mass and size, GCs with more top-heavy IMFs less efficiently produce BBH mergers within the same time interval of evolution.

However, GCs with top-heavy IMFs may maintain the escape velocity highly enough for a long term to keep BHs inside clusters. As a result, the total number of BBH mergers can be large in the case of the top-heavy IMFs (Weatherford et al. 2021). In other words, although the efficiency is low, high-density GCs with top-heavy IMFs can have a longer time to produce BBH mergers. In the case of GCs with top-light IMFs, on the other hand, the total amount of BBH mergers are limited to the total number of BHs, even though they are more efficient.

The comparison with the two-component models from Wang (2020) suggests that the mass loss rate of BHs does not simply depends on the mass segregation time ( $t_{ms}$ ), probably because it is difficult to define an accurate  $t_{ms}$  when a mass spectrum exists. However, the general trend of energy balance (energy flux rate) is consistent with the result of Wang (2020). We also identify the two evolution trend of GCs. BHs escape faster in GCs with the canonical Kroupa (2001) IMF ( $\alpha_3 = -2.3$ ), while light stars are lost faster in the case of top-heavy IMFs (the A1.5 and A1.7 models). The former can finally become dense GCs like observed ones in the Milky-Way galaxy, while the latter become dark clusters with no or very few stars. Since observations can only detect luminous GCs, the contribution of BBH mergers from dark clusters are ignored, but their contribution can be important, as is also discussed in (Weatherford et al. 2021).

## ACKNOWLEDGMENTS

L.W. thanks the financial support from JSPS International Research Fellow (School of Science, The university of Tokyo). M.F. was supported by The University of Tokyo Excellent Young Researcher Program. This work was supported by JSPS KAKENHI Grant Number 17H06360 and 19H01933 and Initiative on Promotion of Supercomputing for Young or Women Researchers, Information Technology Center, The University of Tokyo, and MEXT as “Program for Promoting Researches on the Supercomputer Fugaku” (Toward a unified view of the universe: from large scale structures to planets, Revealing the formation history of the universe with large-scale simulations and astronomical big data). Numerical computations were carried out on Cray XC50 at Center

for Computational Astrophysics, National Astronomical Observatory of Japan.

## DATA AVAILABILITY

The simulation data underlying this article are stored on Cray XC50. The data were generated by the software PETAR, which is available in GitHub, at <https://github.com/lwang-astro/PeTar>. The simulation data will be shared via the private communication with a reasonable request.

## REFERENCES

- Abbott B. P., et al., 2019, *Physical Review X*, 9, 031040
- Abbott B. P., et al., 2020, arXiv, arXiv:2010.14527
- Antonini F., Gieles M., 2019, arXiv, arXiv:1906.11855
- Antonini F., Murray N., Mikkola S., 2014, *ApJ*, 781, 45
- Askar A., Szkudlarek M., Gondek-Rosińska D., Giersz M., Bulik T., 2017, *MNRAS*, 464, L36
- Bae Y.-B., Kim, C., Lee, H. M., *MNRAS*, 440, 2714
- Banerjee S., Kroupa P., 2011, *ApJL*, 741, L12
- Banerjee S., 2020, arXiv, arXiv:2011.07000
- Banerjee S., Belczynski K., Fryer C. L., Berczik P., Hurley J. R., Spurzem R., Wang L., 2020, *A&A*, 639, A41. doi:10.1051/0004-6361/201935332
- Bastian, N. & Lardo, C., 2018, *ARA&A*, 56, 83
- Baumgardt H., Sollima S., 2017, *MNRAS*, 472, 744
- Belczynski K., Bulik T., Fryer C. L., Ruiter A., Valsecchi F., Vink J. S., Hurley J. R., 2010, *ApJ*, 714, 1217. doi:10.1088/0004-637X/714/2/1217
- Belczynski K., et al., 2016, *A&A*, 594, A97
- Belczynski K., et al., 2020, *A&A*, 636, A104
- Breen P. G., Heggie D. C., 2013, *MNRAS*, 432, 2779
- Chatterjee S., Rodriguez C. L., Rasio F. A., 2017, *ApJ*, 834, 68
- Di Carlo U. N., Giacobbo N., Mapelli, M., Pasquato, M., Spera, M., Wang, L., Haardt, F., 2019, *MNRAS*, 487, 2947
- Downing J. M. B., Benacquista M. J., Giersz M., Spurzem R., 2010, *MNRAS*, 477, 1946
- Fryer C. L., Belczynski K., Wiktorowicz G., Dominik M., Kalogera V., Holz D. E., 2012, *ApJ*, 749, 91. doi:10.1088/0004-637X/749/1/91
- Fujii M. S., Tanikawa A., Makino J., 2017, *PASJ*, 69, 94
- Giacobbo N., Mapelli M., 2018, *MNRAS*, 480, 2011
- Giersz M., Askar A., Wang L., Hypki A., Leveque A., Spurzem R., 2019, *MNRAS*, 487, 2412
- Giersz M., Leigh N., Hypki A., Lützgendorf N., Askar A., 2015, *MNRAS*, 454, 3150
- Haghi H., Safaei G., Zonoozi A. H., Kroupa P., 2020, *ApJ*, 904, 43. doi:10.3847/1538-4357/abbfb0
- Hénou M., 1961, *AnAp*, 24, 369
- Hénou M., 1975, *IAUS*, 133, IAUS...69
- Heggie D. C., 1975, *MNRAS*, 173, 729
- Hills J. G., 1975, *AJ*, 80, 809
- Hurley J. R., Pols O. R., Tout C. A., 2000, *MNRAS*, 315, 543
- Hurley J. R., Tout C. A., Pols O. R., 2002, *MNRAS*, 329, 897
- Hong J., Askar A., Giersz M., Hypki A., Yoon S.-J., 2020, *MNRAS*, 498, 4287
- Hosek M. W., et al., 2019, *ApJ*, 870, 44
- Iwasawa M., Tanikawa A., Hosono N., Nitadori K., Muranushi T., Makino J., 2016, *PASJ*, 68, 54
- Iwasawa M., Namekata D., Nitadori K., Nomura K., Wang L., Tsubouchi M., Makino J., 2020, *PASJ*, 72, 13
- Joshi K. J., Rasio F. A., Portegies Zwart S., 2000, *ApJ*, 540, 969
- Kinugawa, T., Inayoshi, K., Hotokezaka, K., Nakauchi, D., Nakamura, T., 2000, *ApJ*, 540, 969
- Kroupa P., 2001, *MNRAS*, 322, 231
- Kumamoto J., Fujii M. S., Tanikawa A., 2019, *MNRAS*, 486, 3942
- Lu J. R., Do T., Ghez A. M., Morris M. R., Yelda S., Matthews K., 2013, *ApJ*, 764, 155
- Marks M., Kroupa P., Dabringhausen J., Pawlowski M. S., 2012, *MNRAS*, 422, 2246
- Mandel, I., de Mink, S. E., 2016, *MNRAS*, 458, 2634
- Marchant P., Langer, N., Podsiadlowski, P., Tauris, T. M., Moriya, T. J., 2016, *A&A*, 588, A50
- Milone A. P., et al., 2017, *MNRAS*, 464, 3636
- Namekata D., Iwasawa M., Nitadori K., Tanikawa A., Muranushi T., Wang L., Hosono N., et al., 2018, *PASJ*, 70, 70. doi:10.1093/pasj/psy062
- O’Leary R. M., Kocsis, B., Loeb, A., 2009, *MNRAS*, 395, 2127
- Oshino S., Funato Y., Makino J., 2011, *PASJ*, 63, 881
- Park D., Kim, C., Lee, H. M., Bae Y.-B., Belczynski K., 2017, *MNRAS*, 469, 4665
- Peters P. C., 1964, *PhRv*, 136, 1224
- Rizzuto F. P., Naab T., Spurzem R., Giersz M., Ostriker J. P., Stone N. C., Wang L., et al., 2020, *MNRAS*.tmp. doi:10.1093/mnras/staa3634
- Portegies Zwart S. F., McMillan S. L. W., 2000, *ApJL*, 528, L17
- Portegies Zwart S. F., Baumgardt H., Hut P., Makino J., McMillan S. L. W.
- Rodriguez C. L., Chatterjee S., Rasio F. A., 2016, *Physical Review D*, 93, 084029
- Rodriguez C. L., Haster C.-J., Chatterjee S., Kalogera V., Rasio F. A., 2016, *ApJL*, 824, L8
- Rodriguez C. L., Morscher M., Wang L., Chatterjee S., Rasio F. A., Spurzem R., 2016, *MNRAS*, 463, 2109
- Rodriguez C. L., Pattabiraman B., Chatterjee S., Choudhary A., Liao W.-keng., Morscher M., Rasio F. A., 2018, *ComAC*, 5, 5. doi:10.1186/s40668-018-0027-3
- Samsing J., Askar A., Giersz M., *ApJ*, 855, 124
- Schneider F. R. N., et al., 2018, *Sci*, 359, 69
- Spitzer L., Hart M. H., 1971, *ApJ*, 164, 399
- Tanikawa, A., 2013, *MNRAS*, 435, 1358
- Tanikawa, A., Susa, H., Yoshida, T., Trani, A. A., Kinugawa, T., 2020, arXiv, arXiv:2008.01890
- Wang L., Spurzem R., Aarseth S., Nitadori K., Berczik P., Kouwenhoven M. B. N., Naab T., 2015, *MNRAS*, 450, 4070
- Wang L., Kroupa P., Takahashi K., Jerabkova T., 2020, *MNRAS*, 491, 440
- Wang L., 2020, *MNRAS*, 491, 2413
- Wang L., Nitadori K., Makino J., 2020, *MNRAS*, 493, 3398
- Wang L., Iwasawa M., Nitadori K., Makino J., 2020, *MNRAS*, 497, 536
- Weatherford N. C., Fragione G., Kremer K., Chatterjee S., Ye C. S., Rodriguez C. L., Rasio F. A., 2021, arXiv, arXiv:2101.02217
- Zhang Z.-Y., Romano D., Ivison R. J., Papadopoulos P. P., Matteucci F., 2018, *Natur*, 558, 260
- Ziosi B. M., Mapelli M., Branchesi M., Tormen G., 2014, *MNRAS*, 441, 3703